Cluster structures in ^{11}B

Tadahiro Suhara
Yukawa Institute for Theoretical Physics, Kyoto University, Kyoto 606-8502, Japan

Yoshiko Kanada-En'yo
Department of Physics, Graduate School of Science, Kyoto University, Kyoto 606-8502, Japan

(Received 7 March 2012; published 29 May 2012)

Structures of excited states in ^{11}B are investigated with a method of β-γ constraint antisymmetrized molecular dynamics in combination with the generator coordinate method. Various excited states with developed cluster core structures are suggested in positive- and negative-parity states. For negative-parity states, we suggest a band with a $2\alpha + t$ cluster structure. This band starts from the $3/2^-_3$ state and can correspond to the experimental band observed recently. In positive-parity states, two α core cluster structures with surrounding nucleons are found. A $K^\pi = 1/2^+$ band is suggested to be constructed from a remarkably developed cluster structure with a large prolate deformation. We discuss features of the cluster structure in association with molecular orbital structures of ^{10}Be.

DOI: 10.1103/PhysRevC.85.054320 PACS number(s): 21.60.−n, 02.70.Ns, 21.10.Ky, 27.20.+n

I. INTRODUCTION

The cluster aspect, as well as the shell-model aspect, are essential features in nuclei. In light nuclei, the cluster and shell-model features often coexist as discussed, for example, for 3α cluster structures in ^{12}C [1–11].

^{11}B can be an interesting nucleus where cluster and shell-model structures coexist. Indeed, it was suggested in previous works that low-lying states of ^{11}B have mainly a shell-model structure [12], while cluster structures develop well in the negative-parity states above or near the threshold [13–15]. Moreover, in a recent experiment of α resonant scattering on ^{7}Li [16], a new negative-parity band consisting of 8.56 MeV ($3/2^-$), 10.34 MeV ($5/2^-$), 11.59 MeV ($7/2^-$), and 13.03 MeV ($9/2^-$) was suggested. Since these states have large α-decay widths, this band is considered to be a band constructed from a cluster structure.

Moreover, cluster features in ^{11}B that are analogous with three α cluster structures in ^{12}C is a fascinating problem to be clarified [14]. In previous works [14,17], the $3/2^-_3$ state was suggested to have a dilute cluster structure with a $2\alpha + t$ configuration and to be analogous with the 0^+_2 state in ^{12}C, which has a dilute 3α structure. However, in recent work [15], it is suggested that ^{11}B($3/2^-_3$) cannot correspond to ^{12}C(0^+_2). The relation between ^{11}B($3/2^-_3$) and ^{12}C(0^+_2) is controversial and further studies for this problem are required. Moreover, for the positive-parity states of ^{11}B, there are few theoretical studies, although cluster states are expected to appear near the threshold energy. Thus, structures of excited states of ^{11}B is a challenging problem to study.

In this article, we investigate structures of excited states in ^{11}B with a certain type of antisymmetrized molecular dynamics (AMD), β-γ constraint AMD, in combination with the generator coordinate method (GCM). To clarify the correspondence between the $3/2^-_3$ state of ^{11}B and the 0^+_2 state of ^{12}C, we compare their GCM amplitudes on the β-γ plane. We also discuss molecular orbital structures with a 2α core and surrounding nucleons for positive-parity states in ^{11}B and their correspondence with ^{10}Be.

This paper is organized as follows. In Sec. II, we explain the framework of the β-γ constraint AMD + GCM briefly. The calculated results are shown in Sec. III. In Sec. IV, we give discussions about structures of ^{11}B. Finally, in Sec. V, we summarize this paper.

II. FRAMEWORK

The frameworks of AMD are described in detail, for example, in Refs. [18–21]. In the present work, we adopt a version of AMD, the β-γ constraint AMD [22], in which we perform the variation with the constraint on the quadrupole deformation parameters, β and γ.

In the method of AMD, a basis wave function of an A-nucleon system $|\Phi\rangle$ is described by a Slater determinant of single-particle wave functions $|\varphi_i\rangle$ as

$$|\Phi\rangle = \frac{1}{\sqrt{A!}} \det\{|\varphi_1\rangle, \ldots, |\varphi_A\rangle\}. \tag{1}$$

The i-th single-particle wave function $|\varphi_i\rangle$ consists of the spatial part $|\phi_i\rangle$, the spin part $|\chi_i\rangle$, and the isospin part $|\tau_i\rangle$ as

$$|\varphi_i\rangle = |\phi_i\rangle|\chi_i\rangle|\tau_i\rangle. \tag{2}$$

The spatial part $|\phi_i\rangle$ is given by a Gaussian wave packet whose center is located at $\boldsymbol{Z}_i/\sqrt{\nu}$ as

$$\langle \boldsymbol{r}|\phi_i\rangle = \left(\frac{2\nu}{\pi}\right)^{\frac{3}{4}} \exp\left[-\nu\left(\boldsymbol{r} - \frac{\boldsymbol{Z}_i}{\sqrt{\nu}}\right)^2 + \frac{1}{2}\boldsymbol{Z}_i^2\right], \tag{3}$$

where ν is the width parameter and is taken to be a common value for all the single-particle Gaussian wave functions in the present work. The spin orientation is given by the parameter $\boldsymbol{\xi}_i$, while the isospin part $|\tau_i\rangle$ is fixed to be up (proton) or down (neutron),

$$|\chi_i\rangle = \xi_{i\uparrow}|\uparrow\rangle + \xi_{i\downarrow}|\downarrow\rangle, \tag{4}$$

$$|\tau_i\rangle = |p\rangle \text{ or } |n\rangle. \tag{5}$$

In a basis wave function $|\Phi\rangle$, $\{X\} \equiv \{\boldsymbol{Z}, \boldsymbol{\xi}\} = \{\boldsymbol{Z}_1, \boldsymbol{\xi}_1, \boldsymbol{Z}_2, \boldsymbol{\xi}_2, \ldots, \boldsymbol{Z}_A, \boldsymbol{\xi}_A\}$ are complex variational parameters and they are determined by the energy optimization.

We perform the variation for the parity projected wave function $|\Phi^{\pm}\rangle$ defined as

$$|\Phi^{\pm}\rangle \equiv \hat{P}^{\pm}|\Phi\rangle, \tag{6}$$

with the constraint on the quadrupole deformation parameters β and γ to obtain various cluster and shell-model structures as the basis wave functions. The definition of β and γ are

$$\beta\cos\gamma \equiv \frac{\sqrt{5\pi}}{3}\frac{2\langle\hat{z}^2\rangle - \langle\hat{x}^2\rangle - \langle\hat{y}^2\rangle}{R^2}, \tag{7}$$

$$\beta\sin\gamma \equiv \sqrt{\frac{5\pi}{3}}\frac{\langle\hat{x}^2\rangle - \langle\hat{y}^2\rangle}{R^2}, \tag{8}$$

$$R^2 \equiv \frac{5}{3}(\langle\hat{x}^2\rangle + \langle\hat{y}^2\rangle + \langle\hat{z}^2\rangle). \tag{9}$$

Here $\langle\hat{O}\rangle$ represents the expectation value of the operator $\hat{O}$ for an intrinsic wave function $|\Phi\rangle$. After the variation with the constraints, we obtain the optimized wave functions $|\Phi^{\pm}(\beta_0, \gamma_0)\rangle$ for each set of parameters, $(\beta, \gamma) = (\beta_0, \gamma_0)$.

In the calculations of energy levels, we superpose the parity and total-angular-momentum projected AMD wave functions $\hat{P}^J_{MK}|\Phi^{\pm}(\beta, \gamma)\rangle$ using GCM. Thus, the final wave function for the $J^{\pm}_n$ state is given by a linear combination of the basis wave functions as

$$\left|\Phi^{J\pm}_n\right\rangle = \sum_K \sum_i f_n(\beta_i, \gamma_i, K)\hat{P}^J_{MK}|\Phi^{\pm}(\beta_i, \gamma_i)\rangle. \tag{10}$$

The coefficients $f_n(\beta_i, \gamma_i, K)$ are determined using the Hill-Wheeler equation.

For the effective two-body interactions, we use the Volkov No. 2 interaction [23] as the central force and the spin-orbit term of the G3RS interaction [24] as the LS force. We take the same interaction parameters as those in Refs. [22,25,26], i.e., the Majorana exchange parameter $M = 0.6$ ($W = 0.4$), the Bartlett exchange parameter $B = 0.125$, and the Heisenberg exchange parameter $H = 0.125$ in the central force and $u_1 = -1600$ MeV and $u_2 = 1600$ MeV in the LS force. These parameters are the same as those adopted in the studies for ^{9}Be [27], and ^{10}Be [28], except for a small modification in the strength of the spin-orbit force to fit the 0^+_1 energy of ^{12}C [22].

For the width parameter of single-particle Gaussian wave packets in Eq. (3), we used the value $\nu = 0.235$ fm^{-2}, which is also the same as those in the studies for C isotopes [22,25,29,30].

III. RESULTS

We performed variational calculations with the β-γ constraint at 196 mesh points of the triangle lattice on the β-γ plane and superposed the obtained wave functions. In this section, we show the calculated results.

A. Energy surfaces

Energy surfaces as functions of β and γ are obtained. We define energy surfaces as the lowest energies after the K-mixing calculation for each (β, γ). The calculated energy surfaces for negative-parity states and those for positive-parity states are shown in Figs. 1 and 2, respectively.

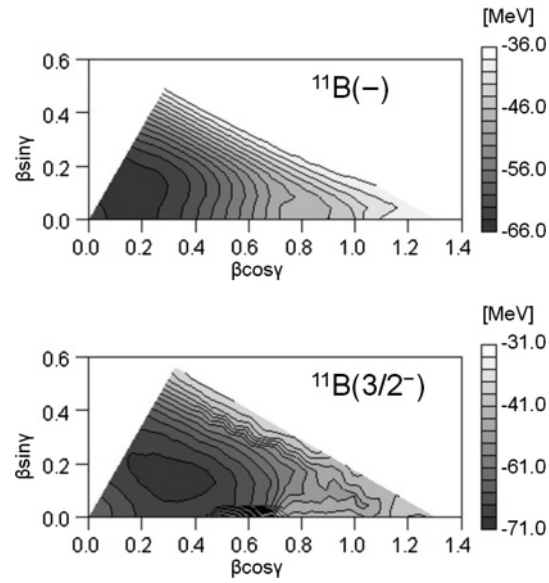

FIG. 1. Energy surfaces of ^{11}B on the β-γ plane. The top panel shows the energy for the negative-parity states and the bottom panel shows that for the $3/2^-$ states after the total-angular-momentum projection.

In Fig. 1, the top panel shows the energy surface for the negative-parity states and the bottom panel shows that for the $3/2^-$ states after the total-angular-momentum projection. We call the former the negative-parity energy surface and the latter the $3/2^-$ energy surface. The minimum point of negative-parity energy surface is at $(\beta\cos\gamma, \beta\sin\gamma) = (0.13, 0.13)$. After the total-angular-momentum projection onto $3/2^-$

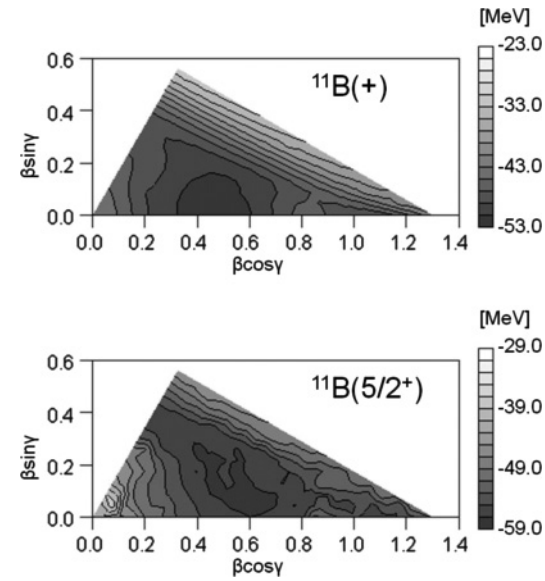

FIG. 2. Energy surfaces of ^{11}B on the β-γ plane. The top panel shows the energy for the positive-parity states and the bottom panel shows that for the $5/2^+$ states after the total-angular-momentum projection.

eigenstates, the minimum point shifts to $(\beta\cos\gamma, \beta\sin\gamma) = (0.33, 0.13)$. This indicates that the deformation of the energy minimum state becomes large after the total-angular-momentum projection. In the large prolate region, a valley is found around $(\beta\cos\gamma, \beta\sin\gamma) = (0.9, 0.1)$. Interestingly, the feature of the $3/2^-$ energy surface for ^{11}B is similar to that of the 0^+ energy surface for ^{12}C (see Fig. 2 in Ref. [22]).

The positive-parity energy surface and the $5/2^+$ energy surface are displayed in the top and bottom panels of Fig. 2, respectively. The minimum point of the positive-parity energy surface is at $(\beta\cos\gamma, \beta\sin\gamma) = (0.45, 0.00)$. After the total-angular-momentum projection onto $5/2^+$ eigenstates, the minimum point shifts to $(\beta\cos\gamma, \beta\sin\gamma) = (0.60, 0.09)$. Thus, the deformation of the energy minimum state changes from the prolate deformation before the total-angular-momentum projection to the large β and triaxial region after the projection. In a largely deformed region, a local minimum exists at $(\beta\cos\gamma, \beta\sin\gamma) = (1.00, 0.00)$ in the positive-parity energy surface and it is at $(\beta\cos\gamma, \beta\sin\gamma) = (1.10, 0.00)$ in the $5/2^+$ energy surface. As we show later, a rotational band with the large prolate deformation is constructed by wave functions in this region after the GCM calculation.

B. Structures on the β-γ plane

In this section, we explain the intrinsic structures of negative- and positive-parity states obtained with the β-γ constraint AMD.

We analyze the spatial configurations of the Gaussian centers $\{\boldsymbol{Z}_1, \boldsymbol{Z}_2, \ldots, \boldsymbol{Z}_A\}$ and the distributions of proton density ρ_p, neutron density ρ_n, and the neutron-proton density difference $\rho_n - \rho_p$ of each intrinsic wave function $|\Phi(\beta,\gamma)\rangle$ obtained for given constraint values, β and γ. The neutron-proton density difference $\rho_n - \rho_p$ shows excess neutron behaviors. We show density distributions $\tilde{\rho}$ which are integrated densities along the y axis as

$$\tilde{\rho}(x,z) \equiv \int dy \rho(\boldsymbol{r}), \tag{11}$$

$$\rho(\boldsymbol{r}) \equiv \langle\Phi(\beta,\gamma)|\sum_i \delta(\boldsymbol{r}-\hat{\boldsymbol{r}}_i)|\Phi(\beta,\gamma)\rangle. \tag{12}$$

The density distributions of the intrinsic wave functions for negative-parity states are illustrated in Fig. 3. Figure 3(a) is the density distribution for the energy minimum state in the $3/2^-$ energy surface $(\beta\cos\gamma, \beta\sin\gamma) = (0.33, 0.13)$. In this wave function, the neutron density has a three-peak structure showing some components of a $2\alpha + t$ cluster structure, though spatial development of the clustering is weak, as indicated by the fact that centers of single-particle Gaussian wave packets gather around the origin. The expectation value of squared intrinsic spin of neutrons is 0.42, which is an intermediate value between 0 for the $2\alpha + t$ cluster limit and 4/3 for the $p_{3/2}$-shell closed configuration limit. This result indicates a mixture of the $p_{3/2}$-shell closed configuration and a $2\alpha + t$ cluster structure. That is to say, this state is considered to be the intermediate between the shell-model structure and the cluster structure.

In the large deformation region, two α and t clusters develop well. Various configurations of clusters appear, depending on the deformation parameters, β and γ. Figures 3(b), 3(c), and 3(d) are typical density distributions for prolate, oblate, and triaxial deformed states, respectively. It is found that the linear-chainlike, equilateral-triangular, and obtuse-angle-triangular configuration arise in the prolate state [Fig. 3(b)], oblate state [Fig. 3(c)], and triaxial state [Fig. 3(d)], respectively.

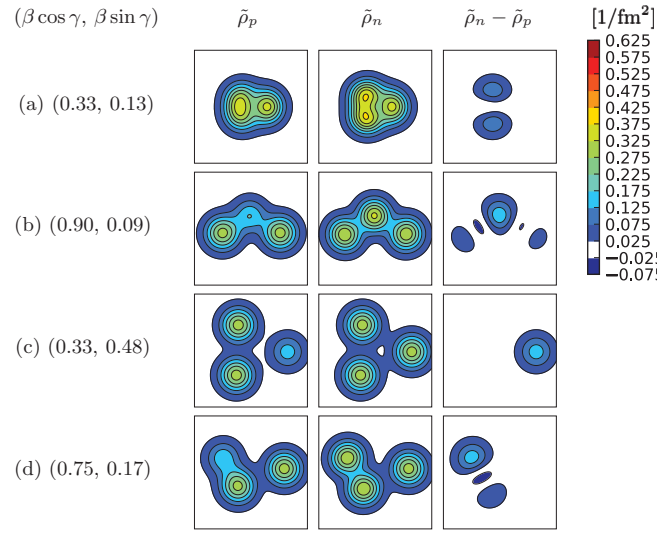

FIG. 3. (Color online) Density distributions of the intrinsic wave functions for the negative-parity states of ^{11}B. The proton density $\tilde{\rho}_p$, neutron density $\tilde{\rho}_n$, and difference between the neutron and proton densities $\tilde{\rho}_n - \tilde{\rho}_p$ are illustrated in the left, middle, and right columns, respectively. The density distributions of the intrinsic wave functions at (a) $(\beta\cos\gamma, \beta\sin\gamma) = (0.33, 0.13)$, (b) $(\beta\cos\gamma, \beta\sin\gamma) = (0.90, 0.09)$, (c) $(\beta\cos\gamma, \beta\sin\gamma) = (0.33, 0.48)$, and (d) $(\beta\cos\gamma, \beta\sin\gamma) = (0.75, 0.17)$ on the β-γ plane are shown. The size of the box is 10×10 fm^2.

Various cluster structures are also found in positive-parity states as well as in negative-parity states. The density distributions of the intrinsic wave functions for positive-parity states are illustrated in Fig. 4. Figure 4(a) shows the density distributions at $(\beta\cos\gamma, \beta\sin\gamma) = (0.60, 0.09)$, which is the energy minimum point of the $5/2^+$ energy surface. In this state, a 2α core is formed. This is seen by the expectation value of the squared proton spin $\langle\hat{S}_p^2\rangle$ is 0.77, which is consistent with the ideal value $\langle\hat{S}_p^2\rangle = 3/4$ for a $2\alpha + t$ configuration where spins of four protons in two α clusters couple to $S = 0$ and one proton in a t cluster gives spin 1/2.

Figure 4(b) shows the density distribution of the local minimum state with $(\beta\cos\gamma, \beta\sin\gamma) = (1.10, 0.00)$ in the $5/2^+$ energy surface. In this state, to be clear from the expectation value of the squared proton spin $\langle\hat{S}_p^2\rangle = 0.80$, a $2\alpha + t$ cluster structure is also formed. In this wave function, three clusters have a linear-chain configuration. After the GCM calculation, a $K^\pi = 1/2^+$ rotational band is constructed from this state, as discussed later.

Figures 4(c) and 4(d) are the density distributions for typical structures with oblate and triaxial deformations in the large β region. In these states, $2\alpha + t$ cluster structures develop well. It is found that the isosceles-triangular structure and obtuse-angle-triangular structure of two α and one t clusters

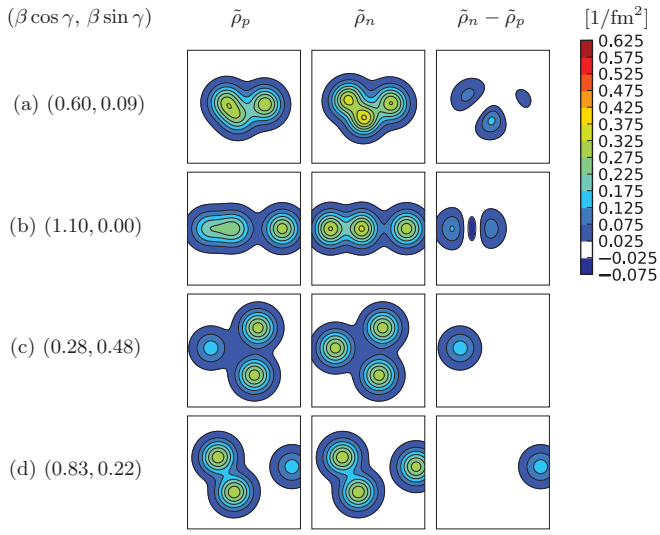

FIG. 4. (Color online) Density distributions of the intrinsic wave functions for the positive-parity states of ^{11}B. The proton density $\tilde{\rho}_p$, neutron density $\tilde{\rho}_n$, and difference between the neutron and proton densities $\tilde{\rho}_n - \tilde{\rho}_p$ are illustrated in the left, middle, and right columns, respectively. The density distributions of the intrinsic wave functions at (a) $(\beta\cos\gamma, \beta\sin\gamma) = (0.60, 0.09)$, (b) $(\beta\cos\gamma, \beta\sin\gamma) = (1.10, 0.00)$, (c) $(\beta\cos\gamma, \beta\sin\gamma) = (0.28, 0.48)$, and (d) $(\beta\cos\gamma, \beta\sin\gamma) = (0.83, 0.22)$ on the β-γ plane are shown. The size of the box is 10×10 fm^2.

arise in the oblate state [Fig. 4(c)] and triaxial state [Fig. 4(d)], respectively.

C. Energy levels

In this section, we describe the results of GCM calculations performed by superposing the obtained wave functions on the β-γ plane for negative- and positive-parity states.

First, we describe the results for the negative-parity states. We show the calculated negative-parity energy levels in Fig. 5 as well as the experimental levels. In the four columns on the left, we display the experimental energy levels for all the negative-parity assigned states [16,32]. In the six columns on the right, the theoretical levels are illustrated. In Fig. 6, we plot the negative-parity energy levels as functions of the angular momentum $J(J+1)$ with $E2$ transition strengths. We also show the calculated $E2$ transition strengths, isoscalar monopole transition strengths, and root-mean-square radii with experimental data [17,31,32] in Tables I, II, and III, respectively. Our calculated results agree with experimental ones reasonably.

With help of $E2$ strengths and analysis of overlaps with basis wave functions, we here describe features of ground and excited states and band structures in the GCM results. The calculated low-lying states have large overlaps with the basis wave functions in the small deformation region. For instance, the $3/2^-_1$ state has 87% overlap with the energy minimum state at $(\beta\cos\gamma, \beta\sin\gamma) = (0.33, 0.13)$ [Fig. 3(a)] in the $3/2^-$ energy surface. As mentioned before, this state has the intermediate feature between the shell-model structure and

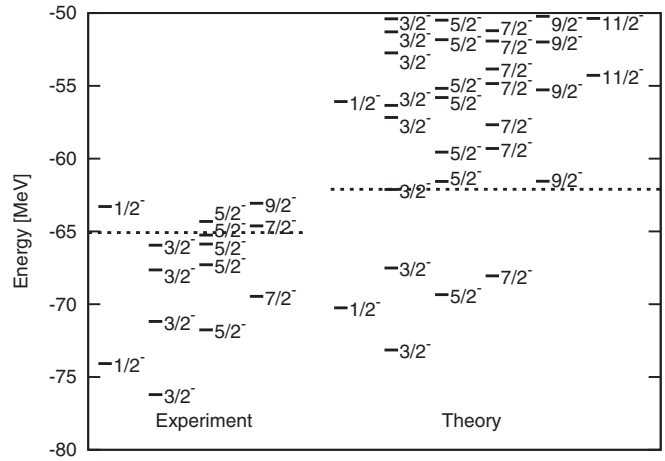

FIG. 5. Energy levels of the negative-parity states in ^{11}B. The four columns on the left are the experimental data and the six columns on the right are the calculated results. The dotted lines in the left and right show the experimental and theoretical $2\alpha + t$ threshold energies, respectively.

the cluster structure. For the low-lying states, the calculated $E2$ strengths are reasonable compared with the experimental values though the level ordering is somehow in disagreement with the experimental one.

In the high-lying states above -65 MeV, we obtain various developed cluster states having significant overlaps with the basis wave functions in the large β regions, such as Figs. 3(b), 3(c), and 3(d). In particular, the $3/2^-_3$ state, which is considered to have a dilute cluster structure with a $2\alpha + t$ configuration, is described by the linear combination of various $2\alpha + t$ spatial configurations. In the next section, we discuss the relation between the $3/2^-_3$ state in ^{11}B and the 0^+_2 state in ^{12}C comparing these GCM amplitudes on the β-γ plane.

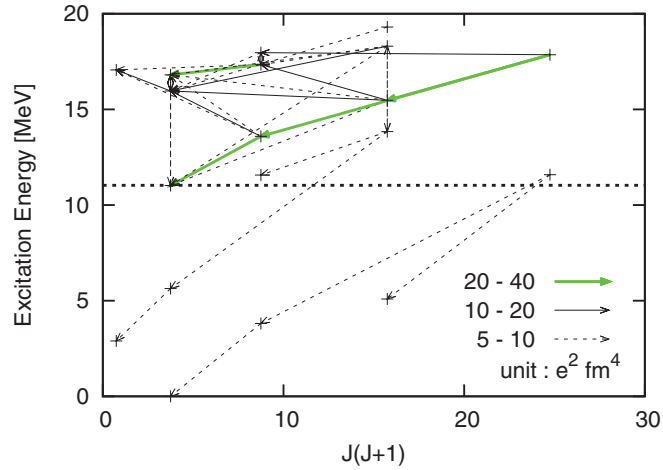

FIG. 6. (Color online) The calculated negative-parity states in ^{11}B against the angular momentum $J(J+1)$ with $E2$ transition strengths. 5.0 e^2 fm^4 $< B(E2) \leqslant$ 10.0 e^2 fm^4, 10.0 e^2 fm^4 $< B(E2) \leqslant$ 20.0 e^2 fm^4, and 20.0 e^2 fm^4 $< B(E2) \leqslant$ 40.0 e^2 fm^4 transitions are described by broken, black solid, and green bold solid arrows, respectively. The dotted line shows the theoretical $2\alpha + t$ threshold energy.

TABLE I. Electromagnetic transition strengths $B(E2)$ for the negative-parity states in ^{11}B. The unit is e^2 fm^4.

Transition	Strength	
	Theory	Experiment
$5/2^-_1 \to 3/2^-_1$	9.2	14 ± 3
$7/2^-_1 \to 3/2^-_1$	1.3	1.9 ± 0.4
$5/2^-_2 \to 3/2^-_1$	0.4	1.0 ± 0.7
$3/2^-_2 \to 1/2^-_1$	6.7	4 ± 3

For the $3/2^-_3$, $5/2^-_3$, $7/2^-_3$, and $9/2^-_3$ states, the $E2$ transition strengths are significantly large as 20–30 e^2 fm^4 (see Fig. 6), and, therefore, we consider these states as members of a band starting from the bandhead $3/2^-_3$ state. In the next section, we discuss the correspondence between this band and the experimental band suggested in Ref. [16].

We next describe the results for the positive-parity states. We show the calculated positive-parity energy levels in Fig. 7 as well as the experimental levels. In the five columns on the left, we display the experimental energy levels for all the positive-parity assigned states [32]. The theoretical levels are illustrated in the six columns on the right.

For the calculated $3/2^+_1$, $5/2^+_1$, $5/2^+_2$, $7/2^+_1$, $7/2^+_2$, $9/2^+_1$, $9/2^+_2$, and $11/2^+_1$ states, we found that these states are constructed dominantly from the AMD wave function at $(\beta \cos\gamma, \beta \sin\gamma) = (0.60, 0.09)$ [Fig. 4(a)], which is the energy minimum of the $5/2^+$ energy surface.

The calculated $1/2^+_1$, $3/2^+_2$, $5/2^+_3$, $7/2^+_4$, $9/2^+_2$, and $11/2^+_2$ states have almost 50% overlap with the AMD base at $(\beta \cos\gamma, \beta \sin\gamma) = (1.10, 0.00)$ [Fig. 4(b)]. As mentioned before, this state has the linear-chain configuration of $2\alpha + t$ clusters. The level spacings of these states show the $K^\pi = 1/2^+$ rotational pattern. Moreover, the calculated $E2$ transition strengths between these states listed in Table IV shows a feature of the $K^\pi = 1/2^+$ rotational band. Namely the transitions in the groups ($1/2^+_1$, $5/2^+_3$, and $9/2^+_3$) and ($3/2^+_2$, $7/2^+_4$, and $11/2^+_2$) are rather strong, while those between the groups are weak. Therefore, we regard the $1/2^+_1$, $3/2^+_2$, $5/2^+_3$, $7/2^+_4$, $9/2^+_3$, and $11/2^+_2$ states as the band members of the $K^\pi = 1/2^+$ rotational band. As will be discussed later, the mechanism why this linear-chain configuration stabilizes and constructs a rotational band can be understood by the molecular orbital structure of the valence $p + 2n$ around 2α clusters, which is analogous to the structures in ^{10}Be. Other states have no specific structure and are difficult to classify as band members.

TABLE II. Isoscalar monopole transition strengths $B(E0; IS)$ for the negative-parity states in ^{11}B. The unit is fm^4.

Transition	Strength	
	Theory	Experiment
$3/2^-_1 \to 3/2^-_2$	2.5	<9
$3/2^-_1 \to 3/2^-_3$	150	96 ± 16

TABLE III. Root-mean-square radii for mass distributions of the negative-parity states in ^{11}B. The unit is fm.

State	Radius	
	Theory	Experiment
$3/2^-_1$	2.29	2.09 ± 0.12
$3/2^-_2$	2.46	
$3/2^-_3$	2.65	

In the present calculation, the $1/2^+_1$ state, which is experimentally known to be the lowest positive-parity state, is missing. It is expected to have $1p$-$1h$ configuration with one proton in the spatial extending $1s_{1/2}$ orbital. Unfortunately, the present framework may not be suitable to describe the spatial extent of $1s_{1/2}$ orbital because the width parameter is taken to be a common value for all the single-particle Gaussian wave functions.

IV. DISCUSSION

A. Negative-parity band from the $3/2^-_3$ state

We here discuss the negative-parity band starting from the $3/2^-_3$ state. As mentioned, the present result suggest the negative-parity band consisting of the $3/2^-_3$, $5/2^-_3$, $7/2^-_3$, and $9/2^-_3$ states (Fig. 6). In the recent experiment of α resonant scattering on ^{7}Li [16], new cluster states were observed, and the negative-parity states at 8.56 MeV ($3/2^-$), 10.34 MeV ($5/2^-$), 11.59 MeV ($7/2^-$), and 13.03 MeV ($9/2^-$) are assigned to be band members. We compare the experimental and calculated band in Fig. 8. Although the calculated excitation energies are higher than experimental ones by 2.5–4.5 MeV, systematics of the level structure, in particular, the small level spacings, correspond well to the experimental ones. Moreover, the present result suggest developed cluster structures in this band and these states probably have large α-decay widths. It supports again that the calculated band can be assigned

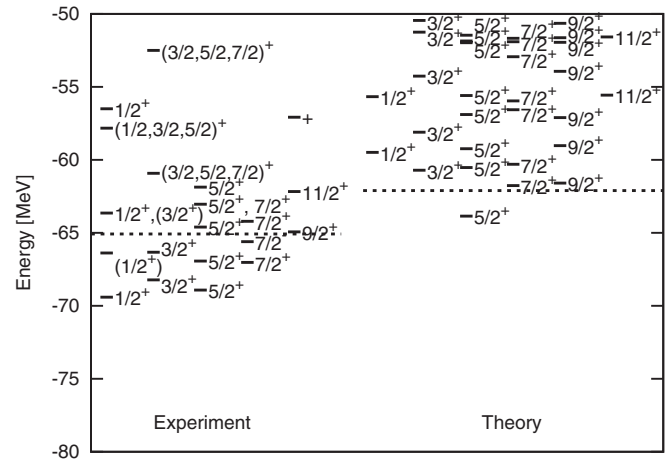

FIG. 7. Energy levels of the positive-parity states in ^{11}B. The five columns on the left are the experimental data and the six columns on the right are the calculated results. The dotted lines in the left and right show the experimental and theoretical $2\alpha + t$ threshold energies, respectively.

TABLE IV. $B(E2)$ for the positive-parity linear states in ^{11}B. The unit is e^2 fm^4.

Transition	Strength
$11/2^+_2 \to 7/2^+_4$	154.8
$7/2^+_4 \to 3/2^+_2$	85.6
$9/2^+_3 \to 5/2^+_3$	84.1
$5/2^+_3 \to 1/2^+_1$	48.6
$11/2^+_2 \to 9/2^+_3$	1.4
$9/2^+_3 \to 7/2^+_4$	6.7
$7/2^+_4 \to 5/2^+_3$	3.8
$5/2^+_3 \to 3/2^+_2$	0.9
$3/2^+_2 \to 1/2^+_1$	10.7

to the experimental band for which large α-decay widths were suggested. To make the correspondence of the calculated states to the experimental observed ones clearer, theoretical estimation of the partial decay widths of the excited states above the $2\alpha + t$ threshold is a remaining future problem.

Cluster structure of the bandhead state, the $3/2^-_3$ state, of this band has been attracting special attention in association with the 0^+_2 state in ^{12}C. In the earlier works [14,17], it is suggested that the $3/2^-_3$ state has a similar feature to the 0^+_2 state in ^{12}C. These states in ^{12}C and ^{11}B are considered to have dilute cluster structures with 3α and $2\alpha + t$ configurations, respectively. To see the similarity of the cluster feature between these states, we compare the GCM amplitude for the $3/2^-_3$ states of ^{11}B with that for the 0^+_2 state of ^{12}C in Fig. 9. The results for the 0^+_2 states in ^{12}C are calculations with the β-γ constraint AMD + GCM taken from Ref. [22]. Fragmentation of the GCM amplitudes for these states is very similar. Both GCM amplitudes spread over the broad γ area of the large β region. In this area of the large β region, the basis wave functions have various configurations of the developed clusters. The feature of the GCM amplitudes indicates that the $3/2^-_3$ state in ^{11}B is described by the linear combination of various $2\alpha + t$ configurations in the same manner as the 0^+_2 state in ^{12}C, which is also described by the linear combination of various 3α configurations. That is, when one α cluster is

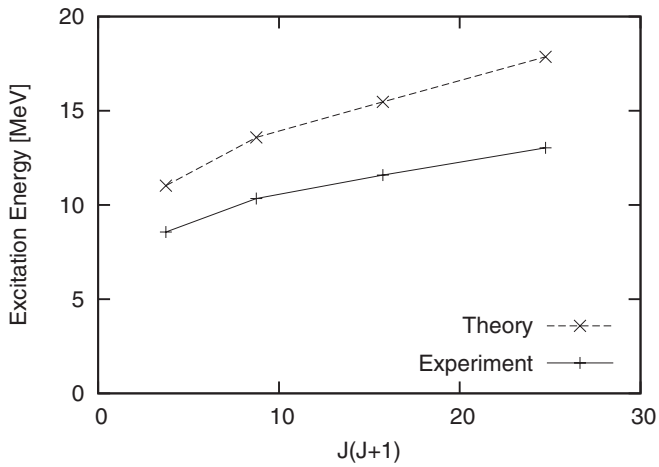

FIG. 8. Comparison between the calculated band ($3/2^-_3$, $5/2^-_3$, $7/2^-_3$, and $9/2^-_3$) and the experimental band suggested in Ref. [16].

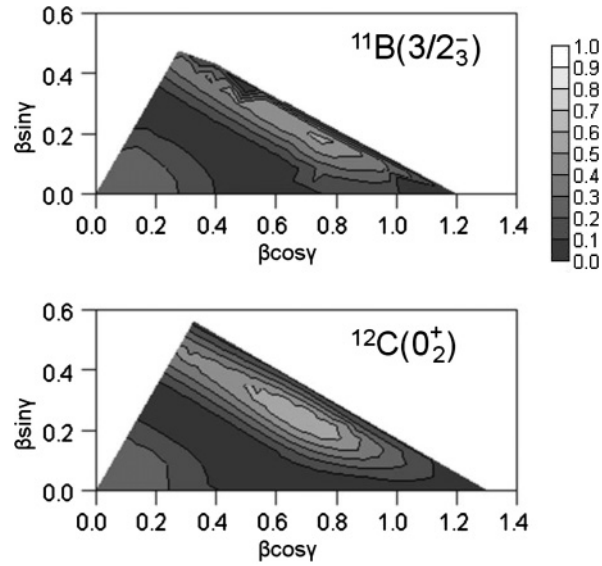

FIG. 9. GCM amplitudes for the $3/2^-_3$ states of ^{11}B and the 0^+_2 states of ^{12}C.

replaced with one t cluster, the structure of the $3/2^-_3$ state in ^{11}B can be regarded as a very similar state to the 0^+_2 state in ^{12}C. Our calculation is consistent with earlier works.

Let us turn again to the level structure of the negative-parity band starting from the $3/2^-_3$ state. As shown in Fig. 8, the energy positions of the $5/2^-_3$, $7/2^-_3$, and $9/2^-_3$ states satisfy the $E_{\rm rot} \propto J(J+1)$ rule of the rigid rotor model, while that of the $3/2^-_3$ deviates from this rule and it is lower than the systematic line. This feature is seen in both the calculated and experimental levels. We here propose a possible reason for the lowering $3/2^-_3$ while focusing on its dilute cluster structure as follows. In the $3/2^-_3$ state, two α and t clusters are weakly interacting, and it may not have a rigid structure. Therefore, the energy cost for rotation of this state can be relatively large. As the angular momentum increases, the structure may change from weakly interacting clusters to a somehow rigid structure with a specific shape, resulting in a larger moment of inertia. By a consequence of the change of moment of inertia, the plot of the energy levels with respect to $J(J+1)$ shows a kink. A similar feature was discussed for the band in ^{16}O, which are considered to start from the 0^+ state just above the four-α threshold, a candidate of the α condensation having weakly interacting four α clusters [33,34].

Here we comment on the behavior of GCM amplitudes except for the $3/2^-_3$ state. As the angular momentum increases, GCM amplitudes gather in the prolate region gradually. Reflecting this behavior, the $5/2^-_3$, $7/2^-_3$, and $9/2^-_3$ states show a rotational nature.

B. Molecular orbital structures in positive-parity states

In this subsection, we introduce an interpretation from the picture of the molecular orbital to discuss structures of positive-parity states and to answer the question why a linear-chain configuration of $2\alpha + t$ clusters stabilize in ^{11}B. Usually a linear-chain configuration is unfavored energetically

because this configuration loses a kinetic energy. Indeed, in the negative-parity states, a superposition of various configurations of $2\alpha + t$ clusters, such as the $3/2^-_3$ state, is favored than a specific configuration of clusters, to gain the kinetic energy of the relative motion of clusters. However, in positive-parity states, the linear-chain configuration of $2\alpha + t$ clusters [Fig. 4(b)] constructs a $K^\pi = 1/2^+$ rotational band as described before. The mechanism of the stabilization can be understood by the molecular orbital picture. In the linear-chain configuration, we consider that one proton and two neutrons occupy the molecular orbitals around two α clusters and spread over the whole system to gain the kinetic energy rather than construct a simple t cluster.

The molecular orbital picture was proposed to describe systems of a 2α core with valence neutron(s) [27,35–39]. Indeed, low-lying states of neutron-rich Be isotopes are successfully described by the molecular orbital pictures [28,36–45]. In a 2α system with valence neutrons, molecular orbitals are formed by a linear combination of p orbits around two α clusters, and valence neutrons occupy the molecular orbitals such as $\pi_{3/2}$ and $\sigma_{1/2}$ orbitals. The $\pi_{3/2}$ orbital ($J^\pi = 3/2^-$) spreads in a direction perpendicular to the axis between α clusters, while the $\sigma_{1/2}$ orbital ($J^\pi = 1/2^+$) spreads parallel to the axis between α clusters. In the ground band of ^{10}Be, valence neutrons have the $(\pi_{3/2})^2$ configuration. While, in the excited states of ^{10}Be, developed cluster structures with other configurations of valence neutrons appear. For instance, the $K^\pi = 1^-_1$ and $K^\pi = 0^+_2$ bands are explained by the $\pi_{3/2}\sigma_{1/2}$ and $(\sigma_{1/2})^2$ configurations, respectively. A molecular orbital model was also applied by Seya *et al.* [36] to B isotopes as well as to Be isotopes.

In the following, we try to explain the structures of the positive-parity states in ^{11}B systematically using the molecular orbital picture. In analogy to the molecular orbital structures in ^{10}Be, we consider ^{11}B to be two α clusters with surrounding a proton and two neutrons which occupy the $\pi_{3/2}$ and $\sigma_{1/2}$ orbitals.

First, we consider the calculated $3/2^+_1$, $5/2^+_1$, $5/2^+_2$, $7/2^+_1$, $7/2^+_2$, $9/2^+_1$, $9/2^+_2$, and $11/2^+_1$ states. The main component of those states is the wave function at $(\beta\cos\gamma, \beta\sin\gamma) = (0.60, 0.09)$ [Fig. 4(a)]. The motion of one valence proton of this wave function can be regarded as the $\pi_{3/2}$ molecular orbitals because one valence proton attach the side of two α clusters and two valence neutrons can be interpreted as occupying $\pi_{3/2}$ and $\sigma_{1/2}$ molecular orbitals. The density distribution of neutrons has a banana shape, which is constructed from the combination of the $\pi_{3/2}$ and $\sigma_{1/2}$ molecular orbitals. As a result, the $3/2^+_1$, $5/2^+_1$, $5/2^+_2$, $7/2^+_1$, $7/2^+_2$, $9/2^+_1$, $9/2^+_2$, and $11/2^+_1$ states can be interpreted as $2\alpha + p(\pi_{3/2}) + 2n(\pi_{3/2}\sigma_{1/2})$. This neutron configuration is similar to that of the $K^\pi = 1^-_1$ band in ^{10}Be.

Next, we discuss the $K^\pi = 1/2^+$ band in ^{11}B. The $K^\pi = 1/2^+$ band is constructed dominantly from the wave function at $(\beta\cos\gamma, \beta\sin\gamma) = (1.10, 0.00)$ [Fig. 4(b)]. In this wave function, protons and neutrons have the elongate structure parallel to the axis between two α clusters. This elongate structure is consistent with the $\sigma_{1/2}$ orbital. Therefore, this wave function can be regarded as $2\alpha + p(\sigma_{1/2}) + 2n[(\sigma_{1/2})^2]$, where a proton and two neutrons occupy the $\sigma_{1/2}$ orbital. The motion of valence neutrons in $K^\pi = 1/2^+$ is similar to that of valence neutrons in the 0^+_2 state of ^{10}Be. Thus, the linear-chain structure of the $K^\pi = 1/2^+$ band in ^{11}B is understood by an extension of the molecular orbital structures in ^{10}Be, namely the linear-chain configuration is stabilized because of valence nucleons in the $\sigma_{1/2}$ orbital.

In the above discussions of molecular orbital structures, we find a good correspondence of the intrinsic structure of positive-parity states in ^{11}B to the excited states in ^{10}Be. In the excited states of ^{10}Be, molecular $2\alpha + 2n$ structures with $\pi_{3/2}\sigma_{1/2}$ and $(\sigma_{1/2})^2$ configurations construct rotational bands. Also in the positive-parity states of ^{11}B, there are two molecular orbital configurations such as $p(\pi_{3/2}) + 2n(\pi_{3/2}\sigma_{1/2})$ and $p(\sigma_{1/2}) + 2n[(\sigma_{1/2})^2]$. That is, the excited states of both nuclei can be described by molecular orbital structures with two α clusters. Note that valence neutrons occupy the same molecular orbitals such as $\pi_{3/2}\sigma_{1/2}$ and $(\sigma_{1/2})^2$ in both nuclei. It suggests that the molecular orbital structures of ^{11}B can be composed by an additional proton and ^{10}Be with the corresponding molecular orbital structures. This correspondence between ^{11}B and ^{10}Be is an interesting result of introducing the molecular orbital interpretation.

Here, we discuss whether other configurations of molecular orbitals exist in ^{11}B. In the simple expectation from the molecular orbital model, other configurations for valence nucleons can appear near or under the $2\alpha + p(\sigma_{1/2}) + 2n(\sigma_{1/2})^2$ states. For example, the $2\alpha + p(\pi_{3/2}) + 2n(\sigma_{1/2})^2$ structure can appear in the negative-parity states because the $\pi_{3/2}$ orbital has lower energy than the $\sigma_{1/2}$ orbital in a simple point of view. However, in the β-γ constraint AMD + GCM calculation, such a state does not appear. We consider the reason for the absence is less correlation energy among nucleons in molecular orbitals. In the $2\alpha + p(\pi_{3/2}) + 2n(\sigma_{1/2})^2$ states, since a valence proton and valence neutrons occupy the different orbitals, they have small spatial overlaps; therefore, valence nucleons gain less correlation energy. However, in the molecular orbital states which appear in the β-γ constraint AMD + GCM calculation, three valence nucleons (a proton and two neutrons) occupy the same orbital and they gain much correlation energy. In other words, the molecular orbital states in which valence proton and neutrons do not occupy same orbitals are unfavored and cannot appear in the low-energy region.

C. Coexistence of shell-model, $2\alpha + t$, and molecular orbital structures

Let us here discuss the coexistence of various structures in ^{11}B. What we find in the present work is two types of cluster structure, three-body $2\alpha + t$ cluster structures and molecular orbital structures, as well as shell-model structures. The $2\alpha + t$ cluster structures in ^{11}B correspond well to the 3α cluster structures in ^{12}C, while molecular orbital structures can be associated with those in ^{10}Be. It should be emphasized that the coexistence of the three-body $2\alpha + t$ cluster and molecular orbital structures is one of the unique features of ^{11}B.

In the ^{11}B system, shell-model structures are seen in the ground and low-lying states, while in the highly excited states near or above the $2\alpha + t$ threshold, three-body $2\alpha + t$ structures and molecular orbital structures with a 2α core are

found. In the molecular orbital structures, the 2α core is formed and three valence nucleons (a proton and two neutrons) are moving in the mean field, i.e., the molecular orbitals around the 2α. It might seem to be contrary to the $2\alpha + t$ structures where a t cluster is formed by correlating three nucleons. The reason why these two kinds of cluster structures coexist in a similar energy region can be explained by the fragility of a t cluster. The binding energy of a t cluster is only 8.5 MeV and much smaller than that of an α cluster. It means that a t cluster can easily break up into three nucleons. In molecular orbital structures, three valence nucleons are in the mean field to gain potential energy from the 2α core. The potential energy gain from the core can compensate the energy loss of the binding energy of a t cluster. As a result, the $2\alpha + t$ cluster and molecular orbital structures coexist in ^{11}B.

As already mentioned, the coexistence of shell-model structures and three-body cluster structures occurs in ^{11}B in a similar way to the coexistence of cluster and shell-model structures in ^{12}C. We then can conclude that shell-model structures, $2\alpha + t$ cluster structures, and molecular orbital ones coexist in the ground and excited states of ^{11}B. This is a coexistence phenomenon peculiar to ^{11}B.

V. SUMMARY

We investigated structures of excited states in ^{11}B with the method of β-γ constraint AMD + GCM. We showed the calculated results for the energy levels, $E2$ transition strengths, isoscalar monopole transition strengths, and a root-mean-square radius, which are in reasonable agreement with experimental data. The present results suggest that the ground and low-lying states have the shell-model structures. In the excited states, well-developed cluster structures are found in the negative- and positive-parity states.

By analyzing the $E2$ transition strengths as well as the GCM amplitudes, we assigned the negative-parity band starting from $3/2^-_3$, in which a $2\alpha + t$ structure develops well. This band is the candidate for a band which was suggested in a recent experiment of α resonant scattering on ^{7}Li. Systematics of the level structure in this band, in particular, the small level spacings, correspond well to the experimental ones. In the experiment, this band is constructed by the states with large α-decay widths. To make the correspondence of the calculated states to the experimental observed ones clearer, theoretical estimation of the partial decay widths of the excited states above the $2\alpha + t$ threshold is a remaining future problem.

In the negative-parity states, the present results suggest a good correspondence of the intrinsic structure with the positive-parity states of ^{12}C as suggested in previous studies. For instance, we found the well-developed $2\alpha + t$ cluster structure of the $3/2^-_3$ state in ^{11}B, which shows similar features to 3α cluster structure of the 0^+_2 state in ^{12}C. In the analysis of GCM amplitudes, we found that the intrinsic structure of the $3/2^-_3$ state in ^{11}B does not have a rigid shape but it is expressed by a linear combination of basis wave functions having various configurations of the developed clusters. The feature is quite similar to the 0^+_2 state in ^{12}C.

For the positive-parity states, a $K^\pi = 1/2^+$ rotational band with a linear-chain configuration of $2\alpha + t$ clusters is suggested. To explain the stabilization mechanism of the linear-chain configuration, we introduced an interpretation from the picture of the molecular orbital. In addition, we discussed a correspondence of the positive-parity states in ^{11}B to the excited states in ^{10}Be. The low-lying states in the positive-parity states of ^{11}B have the $2\alpha + p(\pi_{3/2}) + 2n(\pi_{3/2}\sigma_{1/2})$ structure, which is similar to the $K^\pi = 1^-_1$ band in ^{10}Be $[2\alpha + 2n(\pi_{3/2}\sigma_{1/2})]$ except for the valence proton. The $K^\pi = 1/2^+$ band has the $2\alpha + p(\sigma_{1/2}) + 2n[(\sigma_{1/2})^2]$ structure. This is also similar to the $K^\pi = 0^+_2$ band in ^{10}Be $[2\alpha + 2n(\sigma_{1/2})^2]$.

What we found in the present study of ^{11}B is the coexistence of shell-model, $2\alpha + t$, and molecular orbital structures. Shell-model structures are seen in the ground and low-lying states, while in the highly excited states near or above the $2\alpha + t$ threshold, three-body $2\alpha + t$ structures and molecular orbital structures are found. This is a coexistence phenomenon peculiar to ^{11}B. It is a future problem to investigate other nuclei from the point of view whether this coexistence appears.

ACKNOWLEDGMENTS

We truly appreciate the useful discussions of T. Kawabata and H. Yamaguchi. The computational calculations of this work were performed by use of supercomputers in the Yukawa Institute for Theoretical Physics (YITP) and KEK. This work was supported by the YIPQS program at YITP. It was also supported by a Grant-in-Aid for the Global COE Program "The Next Generation of Physics, Spun from Universality and Emergence" from the Ministry of Education, Culture, Sports, Science and Technology (MEXT) of Japan and a Grant-in-Aid for Scientific Research from the Japan Society for the Promotion of Science.

[1] H. Horiuchi, Prog. Theor. Phys. **51**, 1266 (1974); **53**, 447 (1975).
[2] E. Uegaki, S. Okabe, Y. Abe, and H. Tanaka, Prog. Theor. Phys. **57**, 1262 (1977).
[3] Y. Fukushima and M. Kamimura, J. Phys. Soc. Jpn. **44**, 225 (1978).
[4] P. Descouvemont and D. Baye, Phys. Rev. C **36**, 54 (1987).
[5] Y. Kanada-En'yo, Phys. Rev. Lett. **81**, 5291 (1998).
[6] A. Tohsaki, H. Horiuchi, P. Schuck, and G. Röpke, Phys. Rev. Lett. **87**, 192501 (2001).
[7] Y. Funaki, A. Tohsaki, H. Horiuchi, P. Schuck, and G. Röpke, Phys. Rev. C **67**, 051306(R) (2003).
[8] Y. Funaki, A. Tohsaki, H. Horiuchi, P. Schuck, and G. Röpke, Eur. Phys. J. A **24**, 321 (2005).
[9] T. Neff and H. Feldmeier, Nucl. Phys. A **738**, 357 (2004).
[10] Y. Kanada-En'yo, Prog. Theor. Phys. **117**, 655 (2007).
[11] C. Kurokawa and K. Kato, Nucl. Phys. A **792**, 87 (2007).
[12] P. Navrátil and W. E. Ormand, Phys. Rev. C **68**, 034305 (2003).
[13] H. Nishioka, S. Saito, and M. Yasuno, Prog. Theor. Phys. **62**, 424 (1979).

[14] Y. Kanada-En'yo, Phys. Rev. C **75**, 024302 (2007).
[15] T. Yamada and Y. Funaki, Phys. Rev. C **82**, 064315 (2010).
[16] H. Yamaguchi, T. Hashimoto, S. Hayakawa, D. N. Binh, D. Kahl, S. Kubono, Y. Wakabayashi, T. Kawabata, and T. Teranishi, Phys. Rev. C **83**, 034306 (2011).
[17] T. Kawabata *et al*., Phys. Lett. B **646**, 6 (2007).
[18] Y. Kanada-En'yo and H. Horiuchi, Prog. Theor. Phys. **93**, 115 (1995).
[19] Y. Kanada-En'yo, H. Horiuchi, and A. Ono, Phys. Rev. C **52**, 628 (1995); Y. Kanada-En'yo and H. Horiuchi, *ibid*. **52**, 647 (1995).
[20] Y. Kanada-En'yo and H. Horiuchi, Prog. Theor. Phys. Suppl. **142**, 205 (2001).
[21] Y. Kanada-En'yo, M. Kimura, and H. Horiuchi, C. R. Phys. **4**, 497 (2003).
[22] T. Suhara and Y. Kanada-En'yo, Prog. Theor. Phys. **123**, 303 (2010).
[23] A. Volkov, Nucl. Phys. **74**, 33 (1965).
[24] N. Yamaguchi, T. Kasahara, S. Nagata, and Y. Akaishi, Prog. Theor. Phys. **62**, 1018 (1979).
[25] T. Suhara and Y. Kanada-En'yo, Phys. Rev. C **82**, 044301 (2010).
[26] T. Suhara and Y. Kanada-En'yo, Phys. Rev. C **84**, 024328 (2011).
[27] S. Okabe and Y. Abe, Prog. Theor. Phys. **61**, 1049 (1979).
[28] N. Itagaki and S. Okabe, Phys. Rev. C **61**, 044306 (2000).
[29] N. Itagaki, T. Otsuka, K. Ikeda, and S. Okabe, Phys. Rev. Lett. **92**, 142501 (2004).
[30] N. Itagaki, S. Okabe, K. Ikeda, and I. Tanihata, Phys. Rev. C **64**, 014301 (2001).
[31] A. Ozawa, T. Suzuki, and I. Tanihata, Nucl. Phys. A **693**, 32 (2001).
[32] F. Ajzenberg-Selove and J. H. Kelley, Nucl. Phys. A **506**, 1 (1990).
[33] S. Ohkuboa and Y. Hirabayashi, Phys. Lett. B **684**, 127 (2010).
[34] Y. Funaki *et al*. (to be published).
[35] S. Okabe, Y. Abe, and H. Tanaka, Prog. Theor. Phys. **57**, 866 (1977).
[36] M. Seya, M. Kohno, and S. Nagata, Prog. Theor. Phys. **65**, 204 (1981).
[37] W. von Oertzen, Z. Phys. A **354**, 37 (1996); **357**, 355 (1997).
[38] W. von Oertzen, Nuovo Cimento **110**, 895 (1997).
[39] W. von Oertzen, M. Freer, and Y. Kanada-En'yo, Phys. Rep. **432**, 43 (2006).
[40] A. Dote, H. Horiuchi, and Y. Kanada-En'yo, Phys. Rev. C **56**, 1844 (1997).
[41] Y. Kanada-En'yo, H. Horiuchi, and A. Doté, Phys. Rev. C **60**, 064304 (1999).
[42] K. Arai, Y. Ogawa, Y. Suzuki, and K. Varga, Prog. Theor. Phys. Suppl. **142**, 97 (2001).
[43] N. Itagaki, S. Hirose, T. Otsuka, S. Okabe, and K. Ikeda, Phys. Rev. C **65**, 044302 (2002).
[44] M. Ito, K. Kato, and K. Ikeda, Phys. Lett. B **588**, 43 (2004).
[45] M. Ito, Phys. Lett. B **636**, 293 (2006).